Development of a Soiling Detection for Photovoltaic Modules Based On Static Cameras

Maria Macedo Paz Ferreira
maria.paz.ferreira@tecnico.ulisboa.pt
Instituto Superior Tecnico, Universidade de Lisboa, Portugal, October 2022

Abstract

During the operation of photovoltaic (PV) power plants, soiling reduces the generated power by 3 to 4% on the global average. For quantitative soiling analysis, measurement equipment commercially available covers only small measurement areas. Other published optical measurement methods of soiling use drones. One limitation of these methods is the short duration of the drone flight. This study presents a method to determine the soiling of PV plants over a large area with a high resolution and depending on the PV park, already existing cameras can be used, avoiding extra costs. Commercially available surveillance is used and the method is based on the evaluation of the light scattered by the dirt particles increasing the brightness of the module-soiled areas. The results showed for optimal conditions, a clear sky, the method has a relative deviation to the electrical reference measurement of 2% to 4% and a relative error of 12% to 14% for a clear sky with some clouds. In case of adverse meteorological conditions, the accuracy decreases to 672%.

Keywords

Photovoltaic solar energy, Soiling Measurements, Performance analysis.

Contents

1. Introduction

Soiling in solar energy is the accumulation of snow, dust, leaves, pollen, and bird droppings on PV panels. Generally, dust soiling is the term applied to solid particles with diameters less than 500 μm [1]. Soiling on the PV depends on dust properties, environment, weather conditions, and it is installation design [1]. The knowledge of the degree of soiling enables a more accurate forecast of power plant performance and optimized cleaning strategies [2, 3].

The literature stresses a strong interest and significance in studying PV soiling losses. The initial period includes contributions from the solar pioneers Hottel and Woertz, Tomlinson, [4] who investigated the impact of dust accumulation on solar systems. Garg (1974) (India) [5] study concurred with the fact that horizontal glass receives more dirt than a vertical one. Transmittance values, after sun exposure for horizontal and vertical PV, were found to be 30% and 88%, respectively. Research after the 1990s can be characterized by an integrated nature of investigation augmented with sophistication in experimental rigor resulting in better reliability and accuracy [1]. Mohammad and Fahmy (1993) [5] studied the effect of the physical properties of dust (mainly particle size), and the influence of the amount of dust on the output of a solar panel. Their work showed that smaller particles have a far greater effect than larger particles on the transmittance of glass. Goossens et al. (1993) [6] studied the effect of wind speed on the deposition of dust in Israel. Results showed that even the slightest turbulence in the atmosphere affects the movement of dust particles due to small inertia and under all wind directions, indicating a general increase in dust deposition with an increase in wind speed [1]. Adel (2001) and Hassan et al. (2005) [5] came to a similar conclusion: the speed of decrease in transmittance decreases with time and reaches a saturation point after 30 days of exposure. Elminir et al. (2006) (Egypt) [7] used 100 glass panels with different

tilt angles and measured a dust deposition of $15.84 g/m^2$ (0°) and $4.48 g/m^2$ (90°). Ransome and Sutterlueti (2012) [8] modeled a linear increase in the losses in Madrid (Spain) and how the soiling behavior dominates the cost in regions with long periods without rainfall. Pavan et al. (2011) [9] determined in Italy that the influence of soiling was higher for a 1 MW PV power plant on sandy soil, with 6.9% annual losses, compared to an annual loss of 1.1% for compact soil [5]. Andrews and Pearce (2012) [10] developed a methodology for predicting losses based on readily available meteorological data, especially for snowfall. An extensive part of soiling research is concerned with the effect of dust or soiling at various locations in the world. This information plays a meaningful role in collaboration among researchers and developers [1]. The publications also indicate some trends toward these concerns with mitigation [2, 4].

Since a few years, sensors for integration into the solar field have been available, which determine the soiling on a small measuring area ($< 100 cm^2$) [11, 12]. Another soiling measurement typically used is a pair of PV reference devices, one PV module is continuously clean and the other is naturally soiled. The soiling losses are determined by comparing the output of the soiled reference device with that of the clean one [13]. Afterward, a study conducted by [14] concluded that measurements should be restricted to the middle portion of the day. Thus, excluding high uncertainties from morning and evening hours related to lower signal amplitudes and the effects of angular alignment differences, preferably averaging data for equal periods around the solar noon. Another effect that must be considered, is that moving clouds that may cause the irradiance received may differ between modules. In addition, using PV modules as a reference allows the effect of soiling in the real world, capturing soiling patterns that may not be replicated by smaller work-pieces such as PV cells or glass coupons [15].

One problem with the methods described is the small area covered that is measured in comparison to the solar field. Furthermore, the soiling behavior on the surface of fixed sensors is not necessarily the same as that on the PV panels [11]. There are already publications on the subject of camera-based soiling detection [16]. One article presents a method for quantifying the amount of dust on PV modules by investigating five different image-processing techniques. This study deals with the analysis of color histograms and statistical properties of the captured images of PV modules. An image processing toolbox has been developed using the following techniques: Binarization, Histogram Model, Statistical method, Image Matching, and Texture Matching [15, 16]. In another study, PV module images taken by a camera under laboratory conditions for different dust accumulations detected different features of the gray-level cooperation matrix. The obtained data with new features are classified based on artificial neural networks to determine the dust load and it is influence on PV module performance [17]. However, the approaches listed, have all so far only been tested under laboratory conditions and are still far from large-scale application or commercialization.

A drone camera based in DLR (German Aerospace Center) method is being developed to detect soiling on the PV modules and calculate how much it affects energy production. This method proved to be accurate and served as the foundation of this thesis. The objective of this project is to achieve similar accuracy results using a different camera, a surveillance camera. Not only, a surveillance camera represents a cheaper cost compared to a drone camera case, but also allows one to store more data throughout the day. Lastly, it's flexible, meaning, it is not necessary to wait for good weather (e.g appropriate wind conditions) or to have prior knowledge of how to fly a drone.

2. Camera-Based Method Principles

2.1 Pixel Values to Irradiances

Several mathematical operations are conducted between the CMOS sensor pixel signals and the resulting image [18]. To derive irradiance values, these operations must be partially reversed. A spectral irradiance E_λ falling on a pixel's surface (dA) during the exposure time (t_{exp}) creates the raw signals of the CMOS sensor's pixel. The three signals corresponding to the three color RGB filters are weighted with the camera and color-dependent spectral responsivity written as ε_{nm} and also weighted with a camera-specific 3x3 matrix M_{cam}. Afterward, if there is one, the gamma correction Γ_{sRGB} is applied. The gamma correction is a nonlinear operation adjusting the physical photonic measurements to human perception. Depending on the camera and settings, an offset ($\vec{offset}$) must be added. Thus, the value of a pixel is thus defined by equation 1 [19].

$$\vec{S_{sRGB,mn}} = \Gamma_{sRGB} \cdot \left(\int_{A_{mn}} \int_{\lambda_{min}}^{\lambda_{max}} t_{exp} \cdot \vec{\varepsilon_{nm}} \cdot E_\lambda \, d\lambda \, dA + \vec{offset} \right) \tag{1}$$

A_{mn} is the area of the pixel mn. The pixel (mn) of the RGB image with the three color channels RGB is represented by $\vec{S_{sRGB,mn}}$. λ_{min} and λ_{max} are the minimum and maximum wavelengths of the broadband spectrum, respectively. E_λ denotes the irradiance with wavelengths $\lambda \pm d\lambda$ on sensor area dA before entering the camera. t_{exp} is the exposure time of the camera, which is constant.

In this project, the used camera system is a standard surveillance camera, and the gamma correction applied by the manufacturer is intentionally removed. In addition, each pixel is normalized into the interval [0,1] and converted to grayscale. The grayscale conversion, the normalized color channels, and the weighting factor for each color channel were, done according to P. Kuhn (2017) [19], which used the same camera for his work. The weighting factor for each color channel is calculated from Planck's law [19], and the chosen white balance temperature (10000 K). Thus, the weights of the camera-specific matrix M_{cam} can be reversed. Moreover, the

offset term was photometrically measured and was found to be neglectable [18, 19]. Resulting in the transformed equation 2.

$$S'_{mn} = \vec{\beta_{Planck}} \int_{A_{mn}} \int_{\lambda_{min}}^{\lambda_{max}} t_{exp} \vec{\varepsilon_{nm}} \cdot E_\lambda \, d\lambda \, dA \tag{2}$$

Three further assumptions are made. First, the distribution of the spectral irradiance E_λ is assumed to be homogeneous for the area of each pixel. Thus, the integral over the pixel area A_{mn} is replaced by a constant. Second, ε_{mn} can be different for every pixel but is assumed to be constant over the area of a given pixel (dA) and the considered wavelength spectrum. Thirdly, the broadband irradiance is defined as the weighted integral of E_λ from 280 mn to 4000 mn as specified in Gueymard and Vignola (1998) [20]. With these assumptions and the gamma correction undone, there is linear relation between the broadband (BB) irradiance $E_{BB,mn}$ and the value of pixel (mn) in the linearized grey image S' [19].

$$S'_{mn} = const_{mn} \cdot E_{BB,mn} \tag{3}$$

2.2 Optical Effect of Soiling

Generally, PV modules appear brighter when soiled. Figure 1, is possible to distinguish the cleaned from the soiled module. This assumption is based on the fact that the dirt layer on a PV panel, which depends on the optical properties (size, shape, reflectivity), scatters part of the incident light. The more particles there are per module surface, the more light is scattered, assuming constant illumination conditions. Part of the scattered light is directed toward the surveillance camera, contributing to the pixel RGB value, appearing the PV soiled panel brighter.

A B

Figure 1. Before and after cleaning the PV module. (A) Soiled PV module. (B) Cleaned PV module.

In the case of scattering by particles, both the particle number size distribution and the solar spectrum of the sun play an important role. In addition to scattering, the internal settings of the camera should be taken into account when taking images. Manufacturer corrections make it difficult to compare the images with each other. Thus, the effects of gamma correction, and vignetting are examined for the respective camera. In addition, for the same conditions of soiled conditions, depending on the sun and viewing position the brightness can appear different in the modules. Normally, PV modules appear brighter when viewed from the side. This effect is significantly important for the camera-based methods, due to their variability in sun and camera positions during the recordings, meaning that the brightness of the PV module can be different depending on these two parameters.

Part of the sun radiation that reaches the PV panel is scattered, other is absorbed by the particles or material, and part of the radiation pass through, which is called transmission. The scattering in the direction of surveillance cameras is used to detect the soiling on the PV module. Thus, the RGB image captured value is analyzed pixel by pixel from the corresponding image. Aforementioned in the previous section, the camera has a sensor whose RGB value is proportional to the radiation reaching the pixel sensor, shown in the equation 3 if a few conditions are verified. In addition, the evaluations were conducted on the greyscale image of the red color channel due to the high contrast. This assumption was made based on the fact that PV panels are blue and there is green vegetation around the PV setup. As a consequence, the red color channel shows high contrast, which positively affects the method.

During the camera recordings, it measures the reflections at the module surface, the background of the cell, and scattering due to the soiling layer (Mie-scattering). The equation 4 defines that the irradiance from a soiled module is the sum of the irradiance from a clean module plus an additional scattering term.

$$\begin{aligned} E_{soiled} = E_{clean} \cdot \tau_{soiling}(\alpha_{sun}) \cdot \tau_{soiling}(\alpha_{camera}) \\ + c_{scat}(\vec{r_{sun}}, \vec{r_{camera}}) \cdot E_{scat}(\tau_{soiling}) \end{aligned} \tag{4}$$

E_{soiled} is the radiation reaching the camera from a soiled module. The radiation that reaches the camera sensor if a certain module was cleaned is E_{clean}. The $\tau_{soiling}$ is the optical transmittance of the soiling layer, which is dependent on the sun and camera position. The relative angles α_{sun} and α_{camera} are the angles between the PV panel normal and sun, and the angle between the PV panel normal and camera, respectively. c_{scat} is an empirical function to describe the scattering behavior of the soiling layer in dependence on the sun position and the camera position. Finally, the light scattered at the soiling layer is characterized as E_{scat}, which is dependent on the soiling losses.

This equation was developed by the drone-camera-based method and the main objective of this project is to adapt all the variables to the static-camera case, to solve this equation. Overall, the terms of the equation, in the end, were determined or given by the captured image itself, except $\tau_{soiling}$, the soiling losses. In the beginning, only the initial term, E_{soiled}, is known from the captured image, the total radiation coming from a soiled module to the camera. The following terms were calculated. From the data acquisition, the sun and camera vectors as the respective angles are known. Moreover, the scattering and clean calibrations takes place, to determine the empirical function, c_{scat}, that describes the scattering light on the soiled module and the radiation of a clean module E_{clean}. Lastly, the scattered radiation, E_{scat}, that reaches the camera is dependent on the $\tau_{soiling}$.

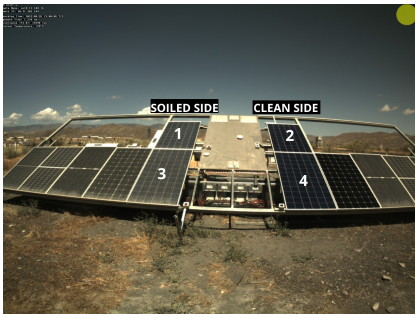

Figure 2. PV setup.Captured image. August 26^{th}.

3. Implementation

3.1 Camera Settings and Layout Configuration

In this project, the cameras used are off-the-shelf standard surveillance cameras (Mobotix MXM24M-Sec-D22, CMOS sensor). Camera settings have been empirically determined once and retained for each recording. This includes, for example, image quality, contrast, and white balance. Automated adjustments recording correction programs that come from the manufacturer have been turned off. Ensuring that the images are as realistic as possible and can be compared. An important setting to be defined is the distance between two shots, i.e time interval between images. After the recordings tests, the time interval was set to 60 seconds due to the variability of the clouds that influence the output. The fixed exposure time used was 1280 microseconds, which is the most suitable for the local conditions.

Figure 2, is a raw image from the surveillance camera perspective and illustrates the PV setup in the desert Tabernas Almería. Overall there are twelve modules in the PV setup, but only the four modules in the center are evaluated in this project due to the technology's compatibility. Each module has an ID number from 1 to 4, illustrated in the image. On one hand, the right side of the PV setup is cleaned every day, modules 2 and 4 are cleaned. On the other hand, modules 1 and 3 are naturally soiled. The four modules have the same technology and are from the same manufacturer. The only difference is the cell type: modules 1 and 2 have 60 cells; modules 3 and 4 have 72 cells. For all the processes and computation, number identification is used as described in figure 2. This layout configuration is fundamental in this work, along with the electrical power output of all modules in the center. Not only plays an important role in calculating the electrical output reference with the module comparison method, but also is essential to perform the clean and scattering calibration.

3.2 Image Corrections

Despite all the settings set in the camera systems, every lens and camera introduce effects in the digital imaging [21]. Hence, influence the soiling evaluation if not corrected. One problem with capturing images is the difference between physical and human perception. The physical perception of the camera sensor is linear. The more light that reaches the camera lens and thus the camera sensor, the higher the measured brightness or voltage at the sensor. Human perception, on the other hand, is not linear. Compared to a camera, the human eye is much more sensitive to changes in dark tones than to similar changes in light tones. Thus, allowing human vision to work over a wider range of luminance. Otherwise, the typical range of brightness encountered outdoors would be too overwhelming. Precisely the gamma correction is a function that relates the pixel's numerical value and it is actual luminance, to compensate for the non-linear luminance effect [21], equation 5 A. For this reason, an attempt is made to reverse the gamma function applied to the images. This is done with the inverse function of the gamma function 5 B.

$$g(x) = f(x)^{\frac{1}{\gamma}} \quad (A), \quad f(x) = g(x)^{\gamma} \quad (B) \tag{5}$$

To obtain the gamma function experimentally, the same subject was photographed with different exposure times. The longer the exposure time, the more light hits the lens and the image becomes correspondingly brighter. For faithful reproduction of the images, the gamma value should be ideally equal to 1, this has been investigated in various publications [21, 22]. Based on this knowledge, the gamma function can be determined experimentally by varying the exposure time.

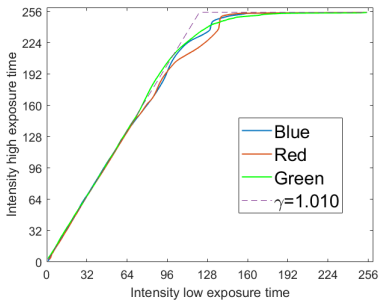

Figure 3. Gamma experiment evaluation graphic.

After the gamma evaluation, it was found that for exposure times higher than 640 microseconds the relationship of the three color channels between the two images with different exposure times, was linear, that is, gamma is equal to 1, figure 3. That is a confirmation that all the settings from the manufacturer are turned off and is not necessary to apply any gamma correction since this project only worked with higher exposure times. However, for lower or dynamic exposure it might be important to take care of this correction before going to the soiling analysis since the system gamma is slightly greater than 1 to improve contrast. Additionally, in the graphic in figure 3, it is possible to observe that for a pixel value higher than 160 it might have some effect causing a systematic deviation in the output. Thus, for heavy soiling, the brightness of the module is higher, and perhaps is necessary to correct the gamma function. In this case, none of the values seen in the data acquisition was higher, so no gamma correction was applied during the project.

In addition, in photography it is common to have a darkening of image corners when compared to the center. This optical effect, called vignetting, occurs in all lenses and depends on the optical design and construction of the lens. It is more notable in lenses with large apertures or barrels. Thus, wide-angle lenses increase the vignetting effect, as the light takes longer to travel from the edge of the lens to the center [19].

This calibration was carried out by measurements with an integrating sphere. The integrating sphere is held in front of the camera lens so that the interior of the integrating sphere is recorded when taking a picture. The light inside the sphere is homogenized by scattering on the inner surfaces. The heterogeneous irradiance recorded by the camera sensor is caused by the attenuation of the camera. However, there were complications to fit the camera inside the integrating sphere due to the protection cape of the camera. Despite all the efforts, the image did not cover the desired area from the integrating sphere. In figure 4 A is possible to see one image from this measurement. To overcome this issue, a mask, figure 4 B, was created during this calibration, identifying: the darker pixels from the borders (range of pixel value 0 to 100); the brighter pixels values, around 255 due to the light source; the yellow dote (recording symbol from the camera system) and the text box located in the upper left corner. In the end, the vignetting evaluation was obtained considering only the pixel values from the integrating sphere, i.e the part not masked in figure 4 B.

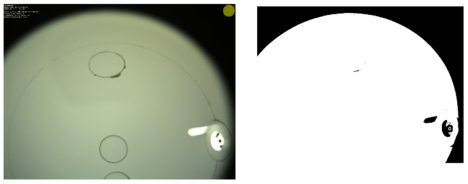

Figure 4. (A) Integrating sphere captured image by the surveillance camera. (B) Ignore mask.

Figure 5 shows the captured normalized vignetting matrix. Afterward, this Vignetting matrix was applied to every image taken for the evaluation. Due to the fit between the camera and the integrating sphere, there is a systematic deviation in the upper part of the matrix. Nevertheless, this was found to be irrelevant, since the upper part of the image taken by the camera is not used.

3.3 System Calibration

If the entire system is considered calibrated, it means that the camera calibration and camera orientation are simultaneously satisfied. Camera calibration is the process of determining the interior orientation parameters [23]. Interior orientation determines the camera's deviation from an ideal one-point perspective model. Deviations arise, for example, from non-ideal lenses and effects on the iris. The parameters to be found by the camera calibration depend on the type of camera used.

Figure 5. Vignetting matrix.

Camera orientation usually includes the determination of the parameters of exterior orientation to define the camera station and camera axis in the higher-order object coordinate system, frequently called the world coordinate system. This requires the determination of three rotational and three translational parameters, in a total of six parameters [23]. Two methods were performed to calibrate the system and compared in the end.

First, the photogrammetry method with the *AICON* software was used. Photogrammetry is the practice of determining the geometric properties of objects from photographic images. This method allows the characterization of geometries with high accuracy but also comes with high preparation effort. This approach represents a complex approach and requires material, time, and knowledge of the software used, resulting in very high precision in the determination of the parameters. Overall, the main effort was to collect images from several perspectives and angles of the structure that were afterward evaluated in the software AICON. In the structure, there are retroreflecting targets (coded and not coded) to highlight the point of interest and a reference system that is indispensable for precise and reliable measurement [23].

The second test was the Chessboard pattern method obtaining high-accuracy measurements of the shape and deformation. The Matlab code provided by Scaramuzza [24, 25, 26], was implemented in this project. This procedure is fast, completely automatic, practical, and no prior knowledge is required [25]. The result of this work is a Matlab Toolbox, which requires minimum user interaction. Thus, it was only necessary to collect between 10 and 20 images of a known pattern, checkerboard, at different positions and orientations [24, 25, 26]. This method assumes that the imaging function can be described by a Taylor series expansion whose coefficients are estimated by solving a four-step least-squares linear minimization problem, followed by a non-linear refinement based on the maximum likelihood criterion [25].

In the end, both methods were compared and it was decided to use the AICON method. Despite similar results, the photogrammetry method has a greater accuracy, which was expected since it is a more complex process. However, it is highly recommended in the future to use the chessboard method due to it is advantages, for example, flexibility and time saving compared to the AICON method.

3.4 Generating Orthoimages

After processing all the images, figure 6 demonstrates all the steps to reach orthoimages.

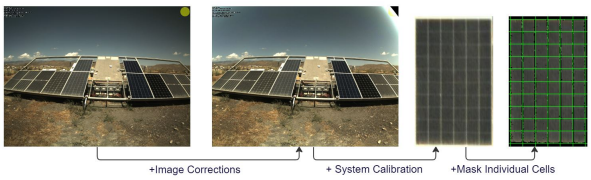

Figure 6. Data processing steps.

The first image is one directly from the data acquisition. It is worth mentioning, that all the settings from the manufacturer were turned off and the exposure time is equal to 1280 microseconds. The next image is the result after applying imaging corrections. In this case, only the vignetting matrix since the gamma value for this exposure time is equal to one. The upper image corners present wrong pixel values due to the drastic change in the vignetting matrix. Fortunately, as aforementioned, it is not relevant to the project, considering that the PV modules are located in the middle of the image and do not contain the strong brightness depicted. Later on, the system calibration is applied, which contains the interior and exterior orientation of the camera, which is required to create orthoimages of the PV Modules. Finally, a mask is created between spaces and conductor lines, to identify cells.

3.5 Data Information and Image Filtering

Before starting there is data treatment throughout all the raw images, processed images, and orthoimages. Obtaining the information needed to calculate the soiling losses at the cell level. Therefore, for each image data, the time stamp and angles are known to describe: the sun position, camera position, solar panel position, and sun rays.

Sun reflection on the images taken by the camera exhibit a general inhomogeneity in brightness. This particular leads to the failure of the estimation of soiling losses since it looks brighter than it is in reality and overestimates the soiling losses. Figure 7 depict modules 2 and 4 at a certain time on the day of August 26^{th}. On one hand, figure 7 A presents sun reflexes. On the other hand, figure 7 B shows an image taken by the camera without sun reflexes. In that way, image filtering takes place before the camera-based method starts to evaluate the images, where it is defined to analyze the image (1, logical value for true) or not analyze the image (0, logical value for false). Excluding from the evaluation the images that present sun reflexes.

3.6 Scattering and Clean Calibrations

Scattering parameters are dependent on the used camera and module technology. For that purpose, a plan was made to determine the scattering parameters with the static surveillance camera. As aforementioned, the brightness of a soiled module changes with the viewing and camera position. To model this behavior, the camera recorded five different positions for six

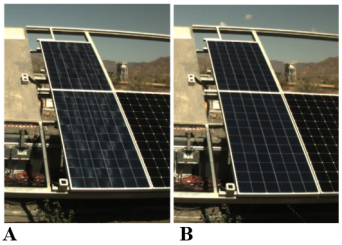

Figure 7. Module 2 and 4, August 26^{th}.(A) - Sun reflex at 13:10:00; (B) - Without sun reflex at 14:00:00.

periods of time on the same day. The different positions of the camera and the module's configuration are depicted in figure 8. For this calibration is necessary to know the energy losses due to soiling in modules 1 and 3 and to have a clean side reference modules 2 and 4. The module comparison method is done, to obtain the exact soiling losses of modules 1 and 3. Moreover, modules 2 and 4 were cleaned, to compare how the brightness changes between a known soiled module and a clean reference module. Thus, an important step in choosing the camera positions was the distance between positions, which is equal to the distance end-to-end of the solar panel 1 and 2 (or 3 to 4), as illustrated by the black line. This ensures that when the camera position is, for example, on position 2 and is evaluating the scattering behavior from the soiled modules (1 and 3), the similar viewing direction for the clean reference modules (2 and 4) corresponds to the camera position 3. To sum up, for each position the program evaluates, it will use the position on the right as a clean reference. In that way, camera position 3 is not used on the scattering behavior because there is not a clean reference for this position. This might be difficult to visualize, but one thing that can be helpful is drawing lines according to the viewing side; both lines need to be parallel. In this case, as illustrated, the scattering behavior of camera position 2 is being evaluated, and the clean reference used is from camera position 3 of the clean modules 2 and 4. The lines are alongside (parallel) and equidistant to the respective modules. The image frequency was 1 image per 15 seconds with a fixed exposure time of 1280 ms (microseconds). In total, over 1000 images were collected, without sun reflexes or other external factors, covering different sun positions during the day from five camera perspectives. The empirical function, c_{scat}, that defines the scattering light on the soiled module is described as dependent on 3 angles: angle camera sun reflex; angle camera panel normal, and angle azimuth camera normal.

Is desirable to have only one scattering calibration at the end of the experiment. However, this was not possible to achieve, since the different modules appeared to have a considerable disparity in energy losses. Although optically the two modules did not show a soiling ratio difference, the electrical output reference calculated revealed to have soiling losses around 2% and 3.5% for modules 1 and 3, respectively. One explanation could be the two bird drops located in module 3. Bird drops cause a decrease in energy efficiency and could result in a miss match between the brightness observed and

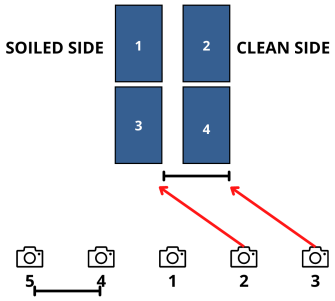

Figure 8. Positions in scattering calibration plan.

the actual energy losses due to soiling (explained in detail in the results section). Other motive, could be a problem in the scattering calibration itself for module 3 or an electrical output reference issue. Hence, two scattering calibrations were made individually and evaluated.

Besides the scattering calibration, the soiling analysis program needs to load a clean calibration for all the modules. The previously discussed calibration plan, scattering calibration, was made precisely to avoid cleaning all the modules from the PV setup. In this way, in parallel with the scattering calibration, the same experiment served as clean calibration. The collected data was made in one clean calibration and like in the scattering calibration, and with Matlab, the brightness of the pixel value, E_{clean}, was defined as dependent on three angles: camera sun reflex, camera panel normal and angle azimuth camera normal.

3.7 Electrical Reference Measurement

Module comparison method is used to obtain the electrical output reference. One side of the PV setup is cleaned and the other side is naturally soiled. With the electrical output of the modules under study, the energy generated is compared and it is possible to know how much energy is wasted due to soiling. In this case, as mentioned before, module 1 is compared to module 2 and module 3 to module 4, due to the different cell types used. In addition, the daytime period used was equal to 1 hour and 15 minutes after and before the solar noon, which is the time when the sun appears to contact the local celestial meridian. In Tabernas desert in August, this time was around 2:15 pm. The sun and PV panels are facing south during this time and the results from this time interval are more reliable because there is no tilted angle influencing the results. Although the compared modules are from the same manufacturer and technology, it is impossible to replicate the same module with the same energy efficiency. Hence, efficiency calibration was done on top of the module comparison method. For that matter, the modules were cleaned and for optimal conditions (clear sky day), the energy generated by the compared modules should be the same. The electrical output showed that module 1 was less efficient than module 2 and module 3 was more efficient than module 4, equation 6.

$$CF_{M1} = \frac{P_{Mc1}}{P_{Mc2}} = 0.99 \quad CF_{M3} = \frac{P_{Mc3}}{P_{Mc4}} = 1.03 \tag{6}$$

CF stands for the correction factor and M for the respective module under study. The P concerns the Power generated and c is to distinguish from a clean or soiled (s) module. Finally, equation 7 shows how the final soiling ratio reference, SR, is obtained for modules 1 and 2 respectively, which contains the module comparison method divided by the correction factor calculated in the efficiency calibration. In addition, a simple mathematical calculation is done to have the soiling losses, SL, in percentage (%), equation 8.

$$SR_M = \frac{P_{Ms}}{P_{Mc}} / CF_M \tag{7}$$

$$SL_M(\%) = 1 - SR_M \tag{8}$$

4. Results

4.1 PV Modules 1 and 2

The period of the images under study was equal to 2 hours and 15 minutes after and before the solar noon (local solar noon 2:15 pm). Table 1 presents an overview of the electrical reference and the results of the camera-based method for all the meteorological conditions tested and the respective absolute and relative errors.

Table 1. Results overview.

	Electrical Reference (%)	Camera-Based (%)	Eabs	Erel(%)
Module 1 - Optimal Conditions				
22^{nd} Aug	6.4	6.5	0.1	2.3
26^{th} Aug	6.7	7	0.3	4.7
15^{th} Sept	1.1	1.1	0.0	2.1
Module 1 - Clear sky with some clouds				
25^{th} Aug	6.3	7.1	0.8	12.6
8^{th} Sept	2.5	2.1	0.4	14.2
Module 1 - Cloudy day				
2^{nd} Sept	1.3	9.7	8.4	672.1

To validate the method and the modeled parameters, optimal meteorological conditions were pursued, that is, a clear sky day. Thus, ensuring there is no influence on the brightness due to clouds and the electrical data presents a smooth power curve over time. Only three days were found in optimal conditions to evaluate the method developed. In this case, both errors, absolute and relative, are small, which indicates that the camera-based method can be validated successfully and used on days with optimal conditions with high accuracy, between 2% and 4%. Generally, the soiling plot displayed in the end of each evaluation, for example, figure 9 are consistent for optimal conditions. Module 2, on the right, as expected, displays dark blue cells, around 0% or minimal soiling losses, since it is cleaned every day. However, lighter dark blue cells exist on the edges and corners, which translates into energy losses. Despite all the efforts to clean the modules, there is a small accumulation of dust on the edges that is very hard or not possible to remove. In addition, the modules in question are difficult to reach, making it not an easy task to clean manually. Regarding the soiled module, there is stronger soiling in the upper part of the module. One thing that can explain this

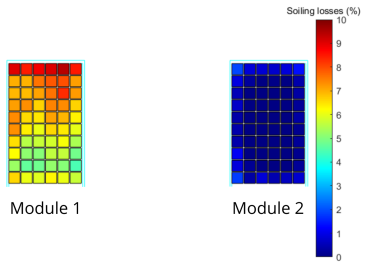

Figure 9. Soiling plot module 1 and 2, 22^{nd} August. Optimal meteorological conditions.

situation is the dust rain from the previous days. Although rain dust also soils the modules, it also has a cleaning effect, since the water goes down with gravity there is more cleaning effect on the lower part of the module. In addition, there is stronger soiling on the edges of the modules, normally dust particles are trapped in the metal edges of the PV panel. Furthermore, for the very first row, 6 cells in the upper part, there might be overexposed pixel values due to the metal edges of the PV panel itself. Thus, might enhance the brightness depicted in the captured image and result in an evaluation error. Nevertheless, the method calculated the soiling losses successfully, and is visible a brightness increase is visible in the upper part of the PV soiled module, due to light scattered by dust particles.

After validating the camera base method, different meteorological conditions were tested, to observe how the results are influenced by diffuse irradiance. The meteorological conditions showed two days with a clear sky and some clouds. The results showed that despite the presence of some clouds, enhancing the diffuse irradiance, can estimate the soiling losses with 12% to 14% of accuracy. Like in the optimal conditions, the soiling plots are consistent and the cleaned modules present minimal losses in the corners and edges. In the soiled module, the upper part presents a higher soiling ratio, this is might be for the same reasons explained before: dust rain and the individual cell mask. The last evaluation performed was on a cloudy day. Here the method's failure under these conditions was witnessed. Not only does the presence of clouds influence the shadows and darker images taken by the camera, but also increases the light scattered and diffuse irradiance. The outcome has a relative error of 672.1%. The soiling plot presented both modules (1 and 2) heavily soiled according to the camera-based method. Like in the previous evaluations, module 2 should appear dark blue with minimal losses in the corners, since it is cleaned every day. Nevertheless, a positive aspect of this evaluation is that, despite module 2 being soiled, the soiling rate compared to module 1 is lower. This is a good direction for future work.

4.2 PV Modules 3 and 4

For modules 3 and 4, all the evaluations showed a relative error above 75%. For that reason, the method failed the validation process.

One possibility behind this situation is the bird drops located in the upper part of module 3. Despite being small, affect the performance of solar PV cells [1]. In addition, the bird drop can cause a electrical miss matched effect, which can play a role on the energy efficiency decrease [27]. This method is not sensible to the electrical model of the PV module. Both soiled modules, 1 and 3, showed similar optical soiling on site. However, module 3 presented higher soiling of 3.5 percent (%) energy losses, a difference of 1,5 percent (%) compared to module 1. This value of 3.5 % relies on energy losses due to soiling and bird drops, but since the bird drops are small compared to the rest of the area of the PV module, the brightness of module 3 almost does not vary compared to the image of module 1. The input of $\tau_{soiling}$, during the scattering calibration will admit that for that specific brightness of the module the energy losses due to soiling are equal to 3.5%. If the empirical function (c_{scat}) to describe the scattering behavior, which is dependent on the camera and sun position, is estimated considering a certain energy loss that is not only caused by mainly dust soiling layer and has a significant impact on the energy losses, like the bird drops, this means that brightness of the module is overestimated in future evaluations.

Another possibility is an unknown problem that occurred during the scattering calibration itself or an issue in the electrical output reference. More efforts are needed to correct this mistake. However, due to time constraints and optimal weather condition dependence, it was not possible to study in depth. Nevertheless, the bird's drop is an interesting topic of study and the theory that is believed to be the origin of the problem in the scattering calibration.

Although the results showed a high inaccuracy when evaluating the soiled module (module 3), the clean module (module 4) displayed an expected value of 0%. This is proof that the inaccuracy of the results is coming from the scattering calibration. No further, evaluations with different meteorological conditions are presented because the method did not pass successfully the validation process for modules 3 and 4.

However, perhaps, if the birds' drops did not exist on the calibration day, meaning that, both modules (1 and 3) would have a similar soiling loss, only one scattering calibration would have been performed. With that being said, if the future evaluation presented a certain brightness and contained bird drops, which not affecting significantly the brightness of the module, an offset could be added to the following equation 4 and calculate the soiling losses with the following equation 9.

$$\tau_{Soiling_{corrected}} = (1 - f_{BD}) \cdot \tau_{soiling} + f_{BirdDrops} \cdot \tau_{BD} \quad (9)$$

$\tau_{SoilingCorrected}$ represents the new soiling losses corrected value calculated with the presence of bird drops in the PV panel. Thus, the sum between the $\tau_{soiling}$ calculated with the camera-based method for the area, which do not contain the bird drops $(1 - f_{BirdDrops})$, and the factor $f_{BirdDrops}$, that is, the fraction between the area occupied by the birds drop divided by the total area of the panel, times the transmission losses of

bird drop $\tau_{BirdDrop}$. Due to time constrains this theory was not possible to be tested, but future work is suggested to overcome this situation.

4.3 Method Limitations

In this work the scattering due to diffuse light is not taken into account, meaning adverse meteorological conditions are a limitation. The shadow variability due to clouds depicted in the captured images and the light scattered influence the outcome of the method, an evaluation of a very cloudy day was made to witness the method's failure. Also, geometries with sun reflexes are avoided due to the overexposed pixel values on the digital image. In that way, image filtering is performed to exclude the unusable image. Moreover, the pixel brightness scales with global illumination in the tilted plane. In addition, although the method calculates the soiling losses at the cell level, the electrical output reference is from the module itself. Thus, the mean value of the soiling losses over all cells is performed and this corresponds to the soiling losses of the module. Furthermore, bird drops were found to be another limitation of this method, especially if the scattering and clean calibrations are performed under these circumstances. Although do not affect substantially the brightness of the soiled module, has an impact on the energy losses. In that way, when calculating the soiling losses with the camera-based method this represents a false perception of the brightness for the rate of soiling losses verified. Lastly, the electrical miss match effect is not taken into consideration in this method. If there is a strong inhomogeneity on the deposited soiling in the PV module or a cell that is strongly soiled, the electrical model needs to be taken into consideration.

5. Conclusions

The validation of the method was successful for modules 1 and 2, obtaining for optimal conditions an accuracy to determine soiling losses between 2% and 4%. The results with different meteorological conditions provided deeper insights into how the variability of the clouds influences the outcome. For the moment, it can be stated that for clear sky conditions or clear sky with some clouds, the method can predict with good accuracy. However, it is worth mentioning that only local soiling/dust from PSA (Plataforma Solar de Almería) was evaluated. If the soiling conditions change, it's necessary to perform a new scattering and clean calibration, because the evaluation is dependent on dust properties. Regarding a very cloudy day, the method accuracy decreases significantly to 672%.

The results from modules 3 and 4 revealed undesirable output and failed the validation process. After a detailed analysis of the module in question, both modules 1 and 3 on-site presented optically the same soiling, which means that both modules should have a similar soiling ratio. The only difference between modules was, module 3 had two bird drops. One possibility behind the wrong calibration is the bird drops located in the upper part of module 3. Despite being small, affect the performance of solar PV cells [1]. Another possibility is an unknown problem that occurred during the scattering calibration or an electrical output reference issue. Nevertheless, the bird's drop is an interesting topic of study and the theory that is believed to be the origin of the problem caused in the scattering calibration. One more limitation needs to be added to the method and future work needs to address this matter. However, for the same evaluation, the clean reference module showed to be accurate and showed 0% of soiling losses. This indicates that the scattering calibration of module 3 is the only wrong input in the method, which overestimates the soiling losses and it is believed that is due to bird drops that significantly influence the energy efficiency outcome, but do not affect the brightness that the camera captures.

A key recommendation is to perform the soiling analysis during the solar noon because there is no title angle influencing the results and the image is clearer. The sun, panels, and camera are facing south and a line can be drawn from the sun until the panels pass through the camera, making it more likely to have direct scattering into the camera. Thus, having sun reflections on the images produces a brightness inhomogeneity in the PV modules. In that way, another proposal is to fix the camera not directly in the center, but on the side, avoiding sun reflexes on the collected data during the solar noon.

Overall, this new camera-based method provides live data, which can be accessed and treated easily. Additionally, it can be used in large areas, for example, a PV park, in contrast to the soiling measurements commercially available [11]. Furthermore, if the PV park already has installed surveillance cameras on site for security or monitoring purposes, it can also be used to evaluate the energy losses due to soiling without needing extra efforts and new installations. Not only, it is used normally for security reasons, but also can be used to optimize the energy efficiency of all parks. In this case, with the soiling analysis evaluations and with a large amount of data, it is possible to optimize the cleaning schedule.

5.1 Outlook

This project demonstrates a valid solution for the detection of soiling in the PV solar energy, and how it can affect the energy efficiency of the process. However, further developments are needed. For one, a larger data set will improve the validation of the extended formula and a sensitivity study will reveal which part of the formula has the greatest potential for improvement. To evaluate a larger data set, it is necessary to have more surveillance cameras installed in the solar plant and/or with a larger overseeing area. Furthermore, recent/modern surveillance cameras are recommended due to their pixel resolution. Due to time constraints, it was only possible to test the model with a fixed exposure time. In this sense, future research should consider dynamic exposure time. Another sensitivity research proposal would be to test this approach for different types of PV modules and various types of soiling.

The last recommendation would be to consider shading by bird drops.

References

[1] Monto Mani and Rohit Pillai. Impact of dust on solar photovoltaic (pv) performance: Research status, challenges and recommendations. *Renewable and Sustainable Energy Reviews*, 14(9):3124–3131, 2010.

[2] Klemens Ilse, Leonardo Micheli, Benjamin W. Figgis, Katja Lange, David Daßler, Hamed Hanifi, Fabian Wolfertstetter, Volker Naumann, Christian Hagendorf, Ralph Gottschalg, and Jörg Bagdahn. Techno-economic assessment of soiling losses and mitigation strategies for solar power generation. *Joule*, 3(10):2303–2321, 2019.

[3] Felix Terhag, Fabian Wolfertstetter, Stefan Wilbert, Tobias Hirsch, and Oliver Schaudt. Optimization of cleaning strategies based on ann algorithms assessing the benefit of soiling rate forecasts. volume 2126, page 220005, 07 2019.

[4] Suellen C.S. Costa, Antonia Sonia A.C. Diniz, and Lawrence L. Kazmerski. Dust and soiling issues and impacts relating to solar energy systems: Literature review update for 2012–2015. *Renewable and Sustainable Energy Reviews*, 63:33–61, 2016.

[5] Reinhart Appels, Buvaneshwari Lefevre, Bert Herteleer, Hans Goverde, Alexander Beerten, Robin Paesen, Klaas De Medts, Johan Driesen, and Jef Poortmans. Effect of soiling on photovoltaic modules. *Solar Energy*, 96:283–291, 2013.

[6] Dirk Goossens. Soiling of photovoltaic modules: Size characterization of the accumulated dust. *Journal of Clean Energy Technologies*, 7:25–31, 05 2019.

[7] Hamdy Elminir, Ahmed Ghitas, Rabab Hamid, Fathy El-Hussainy, M.M. Beheary, and Khaled Abdel-Moneim. Effect of dust on the transparent cover of solar collectors. *Energy Conversion and Management*, 47:3192–3203, 11 2006.

[8] Juergen Sutterlueti, S Ransome, R Kravets, and Ludwig Schreier. Characterising pv modules under outdoor conditions: What's most important for energy yield. 01 2011.

[9] A. Massi Pavan, A. Mellit, and D. De Pieri. The effect of soiling on energy production for large-scale photovoltaic plants. *Solar Energy*, 85(5):1128–1136, 2011.

[10] Rob W. Andrews and Joshua M. Pearce. Prediction of energy effects on photovoltaic systems due to snowfall events. In *2012 38th IEEE Photovoltaic Specialists Conference*, pages 003386–003391, 2012.

[11] Michael Gostein, Stan Faullin, Keith Miller, Jason Schneider, and Bill Stueve. Mars soiling sensor™. *2018 IEEE 7th World Conference on Photovoltaic Energy Conversion (WCPEC) (A Joint Conference of 45th IEEE PVSC, 28th PVSEC & 34th EU PVSEC)*, pages 3417–3420, 2018.

[12] M. Korevaar, J. Mes, and X. van Mechelen. Measuring the sun the components of solar radiation, traceability of measurements, and pv panel soiling. In *Light, Energy and the Environment*, page RTh2B.1. Optica Publishing Group, 2017.

[13] Michael Gostein, Tim Düster, and Christopher Thuman. Accurately measuring pv soiling losses with soiling station employing module power measurements. In *2015 IEEE 42nd Photovoltaic Specialist Conference (PVSC)*, pages 1–4, 2015.

[14] Lawrence Dunn, Bodo Littmann, J. Riley Caron, and Michael Gostein. Pv module soiling measurement uncertainty analysis. In *2013 IEEE 39th Photovoltaic Specialists Conference (PVSC)*, pages 0658–0663, 2013.

[15] Benjamin W. Figgis, Ahmed Ennaoui, Saïd Ahzi, and Yves Rémond. Review of pv soiling measurement methods. *2016 International Renewable and Sustainable Energy Conference (IRSEC)*, pages 176–180, 2016.

[16] Wai Kean Yap, R. P. GALEt, and K. C. Yeo. Quantitative analysis of dust and soiling on solar pv panels in the tropics utilizing image-processing methods. 2015.

[17] Muhammed Unluturk, Ahmet Afşin Kulaksız, and Ali Unluturk. Image processing-based assessment of dust accumulation on photovoltaic modules. *2019 1st Global Power, Energy and Communication Conference (GPECOM)*, pages 308–311, 2019.

[18] Richard Perez, James Schlemmer, Karl Hemker, Sergey Kivalov, Adam Kankiewicz, and Christian Gueymard. Satellite-to-irradiance modeling - a new version of the suny model. In *2015 IEEE 42nd Photovoltaic Specialist Conference (PVSC)*, pages 1–7, 2015.

[19] P. Kuhn, S. Wilbert, C. Prahl, D. Schüler, T. Haase, T. Hirsch, M. Wittmann, L. Ramirez, L. Zarzalejo, A. Meyer, L. Vuilleumier, P. Blanc, and R. Pitz-Paal. Shadow camera system for the generation of solar irradiance maps. *Solar Energy*, 157:157–170, 2017.

[20] C Gueymard and F Vignola. Determination of atmospheric turbidity from the diffuse-beam broadband irradiance ratio. *Solar Energy*, 63(3):135–146, 1998.

[21] Michael D. Grossberg and Shree K. Nayar. What can be known about the radiometric response from images? In Anders Heyden, Gunnar Sparr, Mads Nielsen, and Peter Johansen, editors, *Computer Vision — ECCV 2002*, pages 189–205, Berlin, Heidelberg, 2002. Springer Berlin Heidelberg.

[22] A. Rosebrock. *Deep Learning for Computer Vision with Python: Starter Bundle.* PyImageSearch, PyImageSearch. https://books.google.pt/books?id=9Ul-tgEACAAJ 2017.

[23] Robert Godding. 6 - geometric calibration of digital imaging systems. In Bernd Jähne and Horst Haußecker, editors, *Computer Vision and Applications*, pages 153–175. Academic Press, San Diego, 2000.

[24] Davide Scaramuzza, Agostino Martinelli, and Roland Y. Siegwart. A flexible technique for accurate omnidirectional camera calibration and structure from motion. *Fourth IEEE International Conference on Computer Vision Systems (ICVS'06)*, pages 45–45, 2006.

[25] Davide Scaramuzza, Agostino Martinelli, and Roland Siegwart. A toolbox for easily calibrating omnidirectional cameras. In *2006 IEEE/RSJ International Conference on Intelligent Robots and Systems*, pages 5695–5701, 2006.

[26] D Scaramuzza. Omnidirectional vision: from calibration to robot motion estimation, eth zurich, phd thesis no. 17635., zurich. *ETH Zurich*, 2008.

[27] M. Alonso-Garcia and J.M. Ruíz. Analysis and modelling the reverse characteristic of photovoltaic cells. *Solar Energy Materials and Solar Cells*, 90:1105–1120, 05 2006.